ADVANCED MATERIALS
www.advmat.de

Ultralow Thermal Conductivity, Multiband Electronic Structure and High Thermoelectric Figure of Merit in TlCuSe

Wenwen Lin, Jiangang He, Xianli Su, Xiaomi Zhang, Yi Xia, Trevor P. Bailey, Constantinos C. Stoumpos, Ganjian Tan, Alexander J. E. Rettie, Duck Young Chung, Vinayak P. Dravid, Ctirad Uher, Chris Wolverton, and Mercouri G. Kanatzidis**

The entanglement of lattice thermal conductivity, electrical conductivity, and Seebeck coefficient complicates the process of optimizing thermoelectric performance in most thermoelectric materials. Semiconductors with ultralow lattice thermal conductivities and high power factors at the same time are scarce but fundamentally interesting and practically important for energy conversion. Herein, an intrinsic p-type semiconductor TlCuSe that has an intrinsically ultralow thermal conductivity (0.25 W m^{-1} K^{-1}), a high power factor (11.6 μW cm^{-1} K^{-2}), and a high figure of merit, *ZT* (1.9) at 643 K is described. The weak chemical bonds, originating from the filled antibonding orbitals p-d* within the edge-sharing $CuSe_4$ tetrahedra and long Tl—Se bonds in the PbClF-type structure, in conjunction with the large atomic mass of Tl lead to an ultralow sound velocity. Strong anharmonicity, coming from Tl^+ lone-pair electrons, boosts phonon–phonon scattering rates and further suppresses lattice thermal conductivity. The multiband character of the valence band structure contributing to power factor enhancement benefits from the lone-pair electrons of Tl^+ as well, which modify the orbital character of the valence bands, and pushes the valence band maximum off the *Γ*-point, increasing the band degeneracy. The results provide new insight on the rational design of thermoelectric materials.

1. Introduction

Thermoelectric (TE) materials, which can directly convert waste heat into electricity without moving parts, provide a convenient route of improving energy conversion efficiencies in fossil fuel combustion processes and other sources of heat.[1] One main challenge in TE technology is the low conversion efficiency of TE materials. The efficiency is defined by the figure of merit $ZT = S^2\sigma T/\kappa$, where T is the operating temperature, S is the Seebeck coefficient or thermopower, σ is the electrical conductivity, and κ is the thermal conductivity. Therefore, high ZT is desired for a TE material used in practical applications. However, it is not trivial to increase the ZT of a material because these TE properties are strongly intertwined. In the past decades, many efforts have been devoted to boosting ZT and significant improvements have been achieved by optimizing known TE materials and discovering new

W. Lin, X. Su, C. C. Stoumpos, G. Tan, M. G. Kanatzidis
Department of Chemistry
Northwestern University
Evanston, IL 60208, USA
E-mail: m-kanatzidis@northwestern.edu

W. Lin, J. He, X. Zhang, Y. Xia, V. P. Dravid, C. Wolverton, M. G. Kanatzidis
Department of Materials Science and Engineering
Northwestern University
Evanston, IL 60208, USA
E-mail: c-wolverton@northwestern.edu

X. Su, G. Tan
State Key Laboratory of Advanced Technology for Materials Synthesis and Processing
Wuhan University of Technology
Wuhan 430070, China

The ORCID identification number(s) for the author(s) of this article can be found under https://doi.org/10.1002/adma.202104908.

T. P. Bailey, C. Uher
Department of Physics
University of Michigan
Ann Arbor, MI 48109, USA

C. C. Stoumpos, M. G. Kanatzidis
Department of Materials Science and Technology
University of Crete
Heraklion GR-70013, Greece

A. J. E. Rettie, D. Y. Chung
Materials Science Division
Argonne National Laboratory
Lemont, IL 60439, USA

A. J. E. Rettie
Electrochemical Innovation Lab
Department of Chemical Engineering
University College London
Bloomsbury, London WC1E 6BT, UK

DOI: 10.1002/adma.202104908

TE materials.[2] The widely used strategies of enhancing the power factor (PF = $S^2\sigma$) include band convergence,[3] resonant levels,[4] and quantum confinement effects.[5] On the other hand, defects,[6] solid solutions,[7] nanostructures,[6,8] and hierarchical architectures[9] are commonly utilized to suppress heat transfer through crystal lattices (κ_L). With these strategies, high TE performance has been achieved in many known TE materials such as $AgPb_mSbTe_{2+m}$ (ZT = 2.2 at 800 K),[10] PbTe-4%SrTe (ZT = 2.2 at 915 K),[9] SnSe (ZT = 2.6 at 923 K),[11] FeNbSb (ZT = 1.5 at 1200 K),[12] Cu_2Se (ZT = 2.6 at 850 K),[13] and triple-filled skutterudite (ZT = 1.7 at 850 K).[14] Discovering new TE materials has been largely focused on finding semiconductors with intrinsically low κ_L.[15] In kinetic theory,[16] the κ_L is given by $\kappa_L = \frac{1}{3}C_v v_g^2 \tau$, where C_v, v_g, and τ are the specific heat, phonon group velocity, and phonon relaxation time. The commonly used strategies of minimizing κ_L are to reduce τ through strong anharmonicity,[17] rattling modes,[18] liquid-like ions,[19] et al. and to lower v_g by lattice softening and structural complexity.[20] With these strategies, many semiconductors with ultralow κ_L have been discovered, such as $TlInSe_2$ (0.5 W m^{-1} K^{-1} at 300 K),[21] InTe (0.4 W m^{-1} K^{-1}),[22] SnSe,[11] $CsSnBr_3$ (0.64 W m^{-1} K^{-1} at 300K),[23] and Ag_8SnSe_6 (0.2 W m^{-1} K^{-1} at 300 K)[20b].

There are fewer approaches to improve PF because S and σ have nearly opposite requirements on the electronic band structure. High density of states (DOS), which commonly exists in the less dispersive (flat) bands is important to enlarge the Seebeck coefficient, but leads to low electron mobility and σ. An effective route of solving this contradiction is to increase the band degeneracy (N_v). In a single parabolic band, the density of states effective mass (m^*_d) is related to the band effective mass (m^*_b) through N_v, namely $m^*_d = N_v^{2/3} m^*_b$. A large m^*_d can be achieved in a band with large N_v and small m^*_b. In ionic compounds, the conduction bands and valence bands typically consist of cation-s orbitals and anion-p orbitals respectively, resulting in direct gap semiconductors at the Γ-point, which has the lowest valley degeneracy and low N_v.[20c,24] However, the presence of the lone-pair electrons s^2 of cations can push the valence band maximum and the conduction band minimum away from the Γ-point and significantly increases N_v,[20c,24] as observed in PbTe,[25] BiCuSeO,[26] and Li_2TlBi.[27]

In this work, we describe an intrinsic p-type TE semiconductor TlCuSe with ultralow thermal conductivity (0.25 W m^{-1} K^{-1}), a high power-factor (11.6 μW cm^{-1}), and high ZT (1.9) at 643 K. These favorable properties are a result of the ultralow sound velocity caused by the weak chemical bonds and high band degeneracy originating from the lone-pair electrons of Tl^+. This new TE material presents a unique combination of the ultralow lattice thermal conductivity and high power-factor in a compound with a rather small unit cell. We determine the microscopic mechanisms behind these excellent TE properties, and this understanding can be used to discover and design new TE materials.

2. Results and Discussion

2.1. Crystal Structure and Phase Analysis

TlCuSe crystallizes in the PbClF-type structure (space group $P4/nmm$) with cell parameters of a = 4.0870 Å, c = 8.1950 Å, (**Figure 1**a).[28] The structure shares the same layers of $[CuSe]^{1-}$ as the BiOCuSe compound with the difference being the $[BiO]^{1+}$ sub-layer is replaced by a bilayer of Tl^+ atoms. The Cu atoms are coordinated with four Se atoms forming nearly regular $CuSe_4$ tetrahedra (Se-Cu-Se′ = 110.45°), which are connected with each other by sharing edges, forming antifluorite-type $[CuSe]^{1-}$ layers (Figure 1b). Each Tl atom is located close to the $[CuSe]^{1-}$ layer, surrounded by four Se atoms on its residing layer (Tl-Se = 3.18 Å), adopting a PbO-like connectivity (Figure 1c). The Tl atoms are further weakly bonded to a fifth Se atom in the adjacent layer (Tl···Se′ = 3.87 Å) to form a square pyramid elongated toward its apex. Because of this interaction, the Se atoms themselves adopt an unusual 9-coordinate environment with four Cu atoms and four Tl atoms forming a square antiprism, capped in one of its square faces by a fifth Tl atom from the adjacent layer (Figure 1d). The interlayer interaction is mediated by the stereochemical expression of the $6s^2$ lone pair of Tl^+, which is localized above the empty convex surface defined by the basal Se atoms surrounding Tl, pointing toward the adjacent layer along the crystallographic c-axis (Figure 1e). This situation creates a bilayer of $6s^2$ lone pairs of Tl^+ atoms in the middle of the space between the $[CuSe]^-$ slabs.

Figure 1f presents the powder X-ray diffraction (XRD) pattern of a TlCuSe sample after SPS sintering along with its simulated pattern, indicating that the synthesis product is a pure phase. According to DTA analysis, the compound melts at around 710 K (Figure 1g) without undergoing any solid-state phase transformation. The close temperature spacing between the melting and crystallization peaks attests to the high quality of the sample.

The quality and microstructure of the crystalline sample was further examined by transmission electron microscopy (TEM). Two focused ion beam (FIB)-lift-out TEM specimens were prepared for microstructure characterization along different zone axes. **Figure 2**a,b shows a selective area electron diffraction (SAED) pattern and a high resolution TEM (HRTEM) image of TlCuSe along the [100] direction, respectively. A Wiener filter was applied on Figure 2b to enhance the contrast and remove the contribution of amorphous phases introduced during specimen preparation. Figure 2c,d shows the SAED pattern and HRTEM image of TlCuSe along the [010] direction, respectively. The SAED patterns (Figure 4a,c) match with the simulated diffraction patterns for the $P4/nmm$ space group with no appearance of additional spots, confirming the high crystallinity of the specimens. In Figure 2d, the d-spacing of the (001) plane was measured to be approximately 8.2 Å, which is within reasonable agreement with d_{001} = 8.195(1) Å from the XRD data. Figure 2e shows a representative high angle annular dark field (HAADF) STEM image with corresponding energy dispersive X-ray spectroscopy (EDS) elemental maps of Tl, Cu, and Se. All three elements distribute uniformly throughout the probed region and the uneven contrast in both the HAADF image and elemental maps is mainly due to thickness variation within the characterized area.

2.2. Thermal Transport

Given the quasi 2D nature of the crystal structure of TlCuSe can develop a preferential grain orientation during the

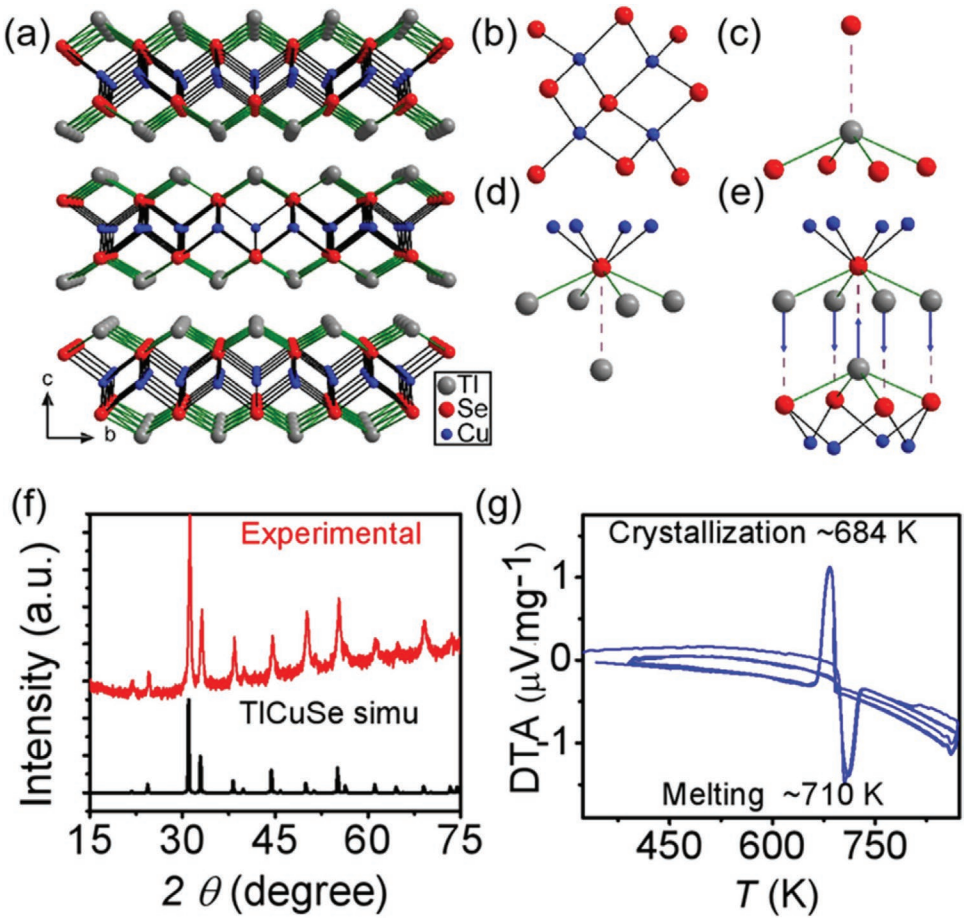

Figure 1. a) Crystal structure of TlCuSe viewed along the *a*-axis. b) Antifluorite-type $[CuSe]^{1-}$ layers. c) Coordination environment of the Tl atom. d) Coordination environment of the Se atom. e) Interlayer interaction between planes of Tl atoms and Se atoms. f) Powder XRD pattern of the TlCuSe sample after the SPS sintering, compared with the simulated XRD pattern of TlCuSe as a black line at the bottom and g) two cycles of DTA thermogram of the TlCuSe sample after the SPS process.

pressing process, we examined the thermal and charge transport properties both parallel and perpendicular to the SPS pressing direction. As shown in **Figure 3**a, the room temperature total thermal conductivities perpendicular and parallel to the pressing direction are 0.70 and 0.44 W m^{-1} K^{-1}, respectively. Both values monotonically decrease with rising temperature and reach 0.40 and 0.25 W m^{-1} K^{-1}, respectively, at 643 K. Figure 3b displays the κ_L derived from the transport data (see Section S1, Supporting Information), indicating that the primary contribution to the total thermal conductivity of TlCuSe is from its lattice. The lattice contribution, κ_L, of TlCuSe are extremely low, 0.20 and 0.28 W m^{-1} K^{-1} for the directions parallel and perpendicular to the pressing direction, respectively, at 643 K. These lattice thermal conductivities are even lower than those of SnSe as well as the Cu-based superionic TE material Cu_2Se.[11,19] For instance, the thermal conductivity of Cu_2Se is 1.0 W m^{-1} K^{-1} at room temperature and drops to 0.7 W m^{-1} K^{-1} at 1000 K.[19] This low κ_L in a compound with a small unit cell is very unusual and we will analyze this behavior next.

To understand the physical origin of the low κ_L, we begin with an analysis of the measured heat capacity data C_p by employing two different models: the Debye model that solely considers the contribution of acoustic phonons and a hybrid one that combines the Debye and the Einstein models including two localized vibrational modes (or Einstein oscillators) in addition to the Debye host. In the hybrid model, the relation between C_p/T and T^2 is expressed as:

$$\frac{C_p}{T} = \gamma + \beta T^2 + \sum_n \left(A_n \left(\Theta_{E_n}\right)^2 \left(T^2\right)^{-3/2} \frac{e^{\Theta_{E_n}/T}}{\left(e^{\Theta_{E_n}/T} - 1\right)^2} \right) \quad (1)$$

In the above equation, the first term corresponds to the electronic contribution, the second term is from the Debye lattice contribution with $\beta = C \times \left(\frac{12\pi^4 N_A k_B}{5} \right) \times (\Theta_D)^{-3}$, where N_A, k_B, Θ_D are Avogadro's number, the Boltzmann constant, and the characteristic Debye temperature, respectively. The parameter C is given as $C = 1 - \sum A_n / 3NR$, where N is the number of atoms per formula unit and R is the gas constant. The third term represents the contribution from the Einstein oscillator modes, where n is the number of Einstein modes, while A_i and Θ_{E_n} are the amplitude and the Einstein temperature of the ith Einstein oscillator mode, respectively.

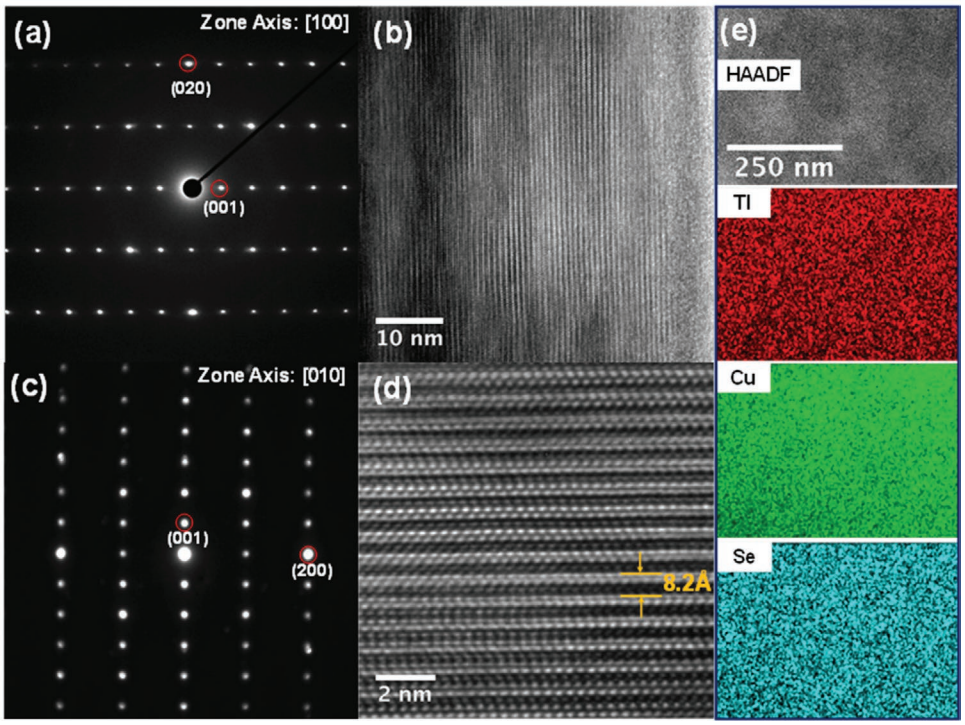

Figure 2. a) Selected area electron diffraction (SAED) pattern and b) high resolution TEM image (with a Wiener filter applied) of TlCuSe along the [100] zone axis. c) SAED pattern and d) high resolution TEM image of TlCuSe along the [010] axis. The highlighted spacing is $d_{001} = 8.2$ Å. e) HAADF STEM image and corresponding elemental EDS maps of TlCuSe. Tl, Cu, and Se distribute uniformly throughout the region of interest. The contrast is due to thickness variation.

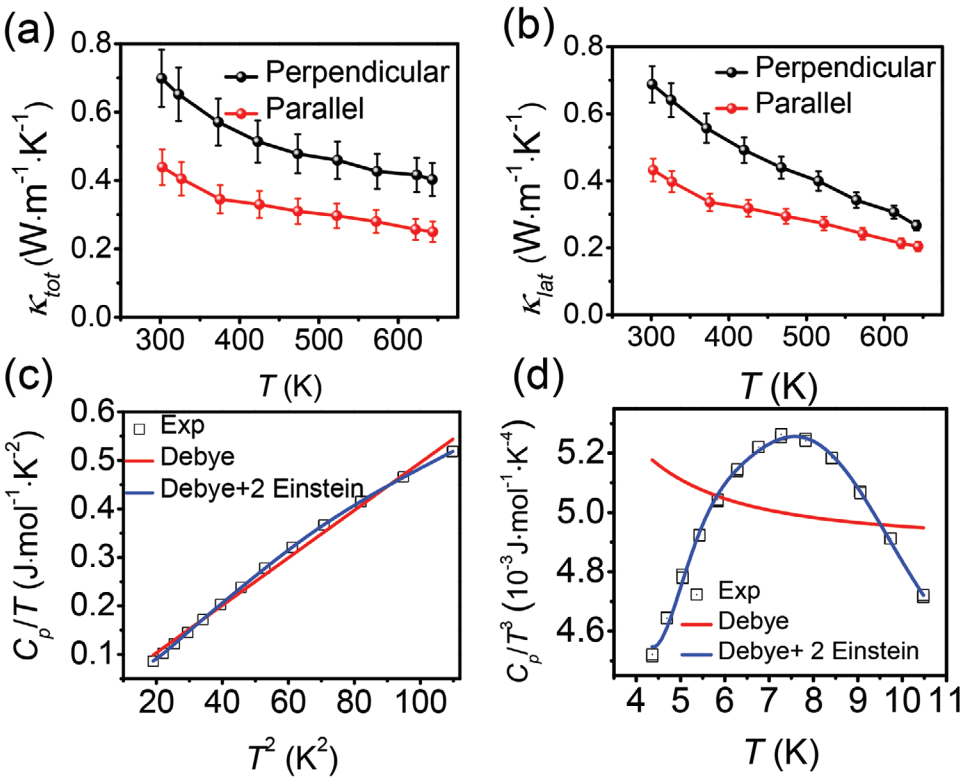

Figure 3. a) Temperature dependence of total thermal conductivity for TlCuSe along two different directions (parallel and perpendicular to the pressing direction) and b) temperature dependence of the lattice thermal conductivity in the two directions for TlCuSe. c) C_p/T versus T^2 with fits shown using just the Debye model and a hybrid model combining both Debye and two Einstein vibrational modes. d) C_p/T^3 versus T with fits shown using just the Debye model and a model incorporating both Debye and two Einstein vibrational modes.

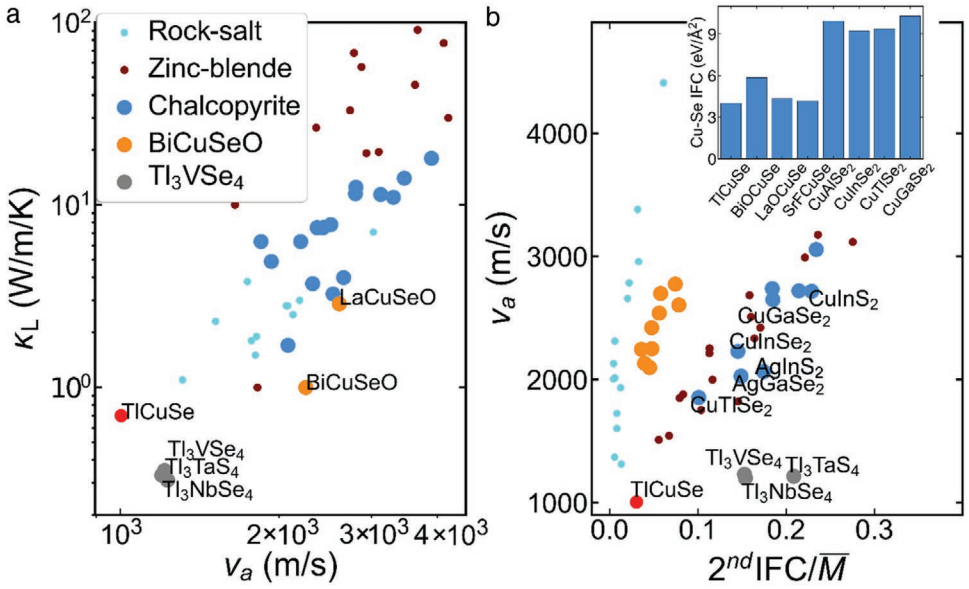

Figure 4. a) Experimentally measured lattice thermal conductivity (κ_L at 300 K) versus computed average sound velocity (v_a) and b) v_a versus the average mass ($\overline{M}$) normalized second-order interatomic force constants (2^{nd}IFC) for compounds with different crystal structures. The size of the dot corresponds to the number of atoms per primitive unit cell. Inset is the force constant between Cu and Se for compounds containing $CuSe_4$ tetrahedra.

Figure 3c shows the relation between C_p/T and T^2 measured between 20 and 110 K. We see that the hybrid Debye + 2 Einstein model fits the experimental data very well (the fitting parameters are given in Table S1, Supporting Information), whereas the Debye model with the conventional T^2 dependence clearly deviates from the data. This observation suggests the possible presence of other excitations, namely low frequency optical phonons, in addition to the acoustic phonon modes. Moreover, as shown in Figure 3d, a broad peak appears in the experimentally measured C_p/T^3 versus T relation, which deviates considerably from the Debye model, but can be very well recovered using a hybrid Debye +2 Einstein model. This type of peak is often found in low temperature heat capacity data of disordered glasses, as well as in clathrates and skutterudites, and has been attributed to the excess phonon density of states (DOS) resulting from guest-induced low-lying optical modes.[29]

In TlCuSe, the excess contribution to C_p at low temperatures may be associated with the low-energy optical modes from the weakly bound Cu^+ and rattling-like Tl^+ ions, which will be discussed in detail in the subsequent section. It has been pointed out in recent studies that these low-lying optical modes coupled with heat-carrying acoustic modes not only reduce the v_g but also enhance phonon scattering (τ^{-1}), thus leading to the observed ultralow κ_L.[30] Similar phenomenon has been observed in several other materials such as $(Bi,Sb)_2Te_3$, MgAgSb, Cu_3SbSe_3, and $TlInTe_2$,[21,31] all of which exhibit intrinsically very low thermal conductivity.

A key factor that we find contributes to the very low thermal conductivity in TlCuSe is its very low average sound velocity (v_a) of about 886 m s^{-1}, which is the long wavelength limit of v_g and can be calculated from the fitted Debye temperature (Θ_D = 94.4 K, see Table S1, Supporting Information). To the best of our knowledge, this is the lowest v_a among the known TE materials (the previous one with the lowest v_a is Ag_8GeTe_6 is 1009 m s^{-1}).[20b,32] To further illustrate this, we show in **Figure 4**a the experimentally measured κ_L and our density functional theory (DFT) calculated v_a for the semiconductors with several common crystal structures. Note that these DFT calculated v_a might be slightly larger than the measured values due to the presence of thermal expansion and defects in the synthesized samples and the approximations due to the exchange-correlation functional (PBEsol) in the DFT calculations. As expected, we see a strong correlation between v_a and κ_L. In particular, small v_a is usually associated with small κ_L and vice versa, especially within the same category of crystal structure. On the other hand, the crystal structure also plays an important role in determining κ_L, for example rock-salt compounds tend to have smaller κ_L than those of the zinc-blende compounds exhibiting similar values of v_a, due to different phonon–phonon scattering rates in these two structures.[33] We see that among these compounds, TlCuSe has the lowest v_a and a very low κ_L, whose values are close to those of Tl_3MX_4 (M = V, Nb, and Ta; X = S and Se).[34] These Tl-based chalcogenides are known to have the lowest κ_L among compounds with relatively simple structures and a small number of atoms in the unit cell. This indicates that the mechanism behind the low v_a reported here is sharply different from that of crystal structures with large/complex unit cells.[35] It is even more intriguing to notice that although many other Cu–Se compounds also have low κ_L, as shown in Figure S1, Supporting Information, TlCuSe has a much simpler crystal structure and smaller unit cell.

To explore the origin of the low v_a in TlCuSe, we plot v_a versus the second-order interatomic force constant normalized by the average mass ($2^{nd}IFC/\overline{M}$) of the compounds with common crystal structures in Figure 4b. TlCuSe has a smaller $2^{nd}IFC/\overline{M}$ than all the other compounds except a few with the rock-salt structure, which generally has a small IFC (weak bonding interaction) due to its high coordination number.[20c] The large value

of $\overline{M}$, due to Tl, and the small 2ndIFC indicates weak bonding between the constituent atoms in TlCuSe. The weak Tl—Se bond can be seen from its long bond length (3.18 Å), which is commonly observed in Tl^+ compounds such as Tl_3MSe_4 (M = V, Nb, and Ta). Interestingly, we find that the Cu—Se bond in TlCuSe is also very weak. As we can see from the inset of Figure 4b, the 2ndIFC between Cu and Se in TlCuSe is nearly three times smaller than that in chalcopyrite (with corner-sharing $CuSe_4$ tetrahedra), but is comparable with that in the BiCuSeO-type structure, (with edge-sharing $CuSe_4$ tetrahedra in the layer direction), the same as TlCuSe. This observation is consistent the Pauling's third rule that the sharing of edges and faces by two polyhedra substantially decreases the stability (elongates cation–anion bond length) of an ionic structure, due to the Coulomb repulsion between cations in two adjacent polyhedra.[36] Indeed, the Cu—Se bond length in TlCuSe and BiCuSeO (≈2.5 Å) is longer than that in chalcopyrite (≈2.4 Å). We can also understand the weak Cu—Se bond in terms of the electronic structure. Cu—Se bonds in all these compounds have anti-bonding orbitals below the Fermi level due to the unusual d–p coupling between Cu-3d and Se-4p orbitals,[37] see crystal orbital Hamilton population (COHP) analysis for these compounds in Figure S2, Supporting Information. The filling of the anti-bonding states decreases the bond order and destabilizes the Cu—Se bond, thus leading to weak interatomic interactions, which may partially explain why Cu^+-based semiconductors have low κ_L in general.[38] Our analysis reveals that weak Cu—Se and Tl—Se bonds and heavy atomic masses can be viewed as the major origin of the low v_a in TlCuSe.

2.3. Phonon Dispersion

To gain more insight into the lattice dynamics in TlCuSe, we performed phonon calculations based on DFT force constants. The phonon dispersion curves in the first Brillouin zone and the corresponding projected density of states (PDOS) at 0 K are shown in Figure 4a. The phonon dispersion shows that there are small imaginary frequencies at M ($M_1 \approx 13i$ cm^{-1}) and along the line between Γ and X ($\Delta_1 \approx 10i$ cm^{-1}). We have confirmed that these imaginary frequencies are independent on the choice of exchange-correlation function and displacement amplitude of phonon calculations (see Figure S3, Supporting Information). The atom displacement of the M_1 mode, reveals that the Cu^+ cation exhibits much larger amplitudes than all other atoms, see Figure S4, Supporting Information. Moreover, we find that displacing the atoms along the eigenvectors of the unstable M_1 mode leads to a subgroup structure *Pbcm* only 2 meV per atom lower than the observed *P*4/*nmm* phase. The small imaginary frequency and energy difference indicate that any phase transition from *Pbcm* to *P*4/*nmm* is likely at very low temperature and only the *P*4/*nmm* structure can be observed at room temperature, which is consistent with the experimental observation. We note that investigating the behavior of these imaginary phonon modes at finite temperatures is certainly of great interest, but beyond the scope of current study, which will be left for a future study. The PDOS shows that the low-frequency phonon branches (≈18 cm^{-1}) are mainly from the Tl, due to its heavy mass and weak Tl—Se bond. Although Cu has the smallest atomic mass in TlCuSe, Cu does have a remarkable contribution to the low-frequency modes as well, which can be clearly viewed from the large atom displacements in real space, see Figure S4, Supporting Information. This is consistent with the weak Cu—Se bond in the edge-sharing $CuSe_4$ tetrahedra as discussed before. Finally, the low frequencies of acoustic phonons along Γ-Z direction originate from the weak interlayer bonding interactions.

Since Tl^+ has lone-pair electrons ($6s^2$), we study the impact of lone-pair electrons on the potential energy surface (PES) by displacing Tl along the *c*-axis (the direction that the lone-pair electrons pointing toward), comparing with Rb^+ in the same structure, which has similar ionic radius but no lone-pair electrons. The PES of Tl atom has lower energy and stronger anharmonicity (the 3rd-order onsite force constant is 0.51 eV Å^{-3}) than those of Rb (the 3rd-order onsite force constant is 0.18 eV Å^{-3}), which is evidence of the effects from the lone-pair electrons. The electron localization function in **Figure 5**b clearly indicates the lone-pair electrons of Tl^+ pointing along the *c*-axis. Strong anharmonicity significantly increases the phonon–phonon scattering rate and reduces phonon relaxation time (τ). Therefore, we find that the ultralow κ_L of TlCuSe originates from the low phonon velocity (v_a) and short phonon lifetime (τ).

2.4. Electronic Band Structures

The calculated electronic band structure and projected density of states (PDOS) of TlCuSe are shown in Figure 5c, along with the first Brillouin zone of the *P*4/*nmm* space group in Figure 5d. It is clear that TlCuSe has a multiband character which is highly beneficial to its PF. The HSE06 calculated band gap, including spin-orbit coupling (SOC), is 0.59 eV, in good agreement with the activation energy derived from the temperature-dependent carrier concentration (**Figure 6**f). The valence band maximum (VBM) is located in the middle of the S line (along *A*-*Z*) in the first Brillouin zone and has a band degeneracy (valley degeneracy × energy degeneracy) of N_v = 4. The second and third maxima are along the Σ (N_v = 4) and U (N_v = 4) lines, sitting 194 and 310 meV lower than the VBM, respectively. Thus, hole doping and temperature broadening of the Fermi level can generate carriers from multiple regions of reciprocal space. The calculated band effective mass (m_d^*) of the hole (electron) along *A*-*Z* direction is 0.3 (0.2) m_0, indicating a high carrier mobility. The DOS effective mass (m_b^*) of holes and electrons are enlarged by the high band degeneracy as $m_d^* = N_v^{2/3} m_b^*$, which can enhance the Seebeck coefficient without impairing the electrical conductivity.[39] The multiband character of TlCuSe derives from the hybridization between the filled 6s lone-pair-electrons, empty 6p orbitals in Tl^+ and filled 4p orbitals of Se. This hybridization can be better illustrated by comparing and contrasting with the band structure of NaCuSe which has the same structure and CuSe layer but the Na^+ has no lone-pair-electrons. In NaCuSe both VBM and CBM occur at the Γ point. As shown in Figure S5, Supporting Information, the hybridization between the 6s-orbitals of Tl^+ and the 4p-orbitals of Se shifts the VBM from Γ to the middle of the S line since the s-like band always increases from the Γ point (σ bonding between s-orbitals) to the Brillouin zone boundary

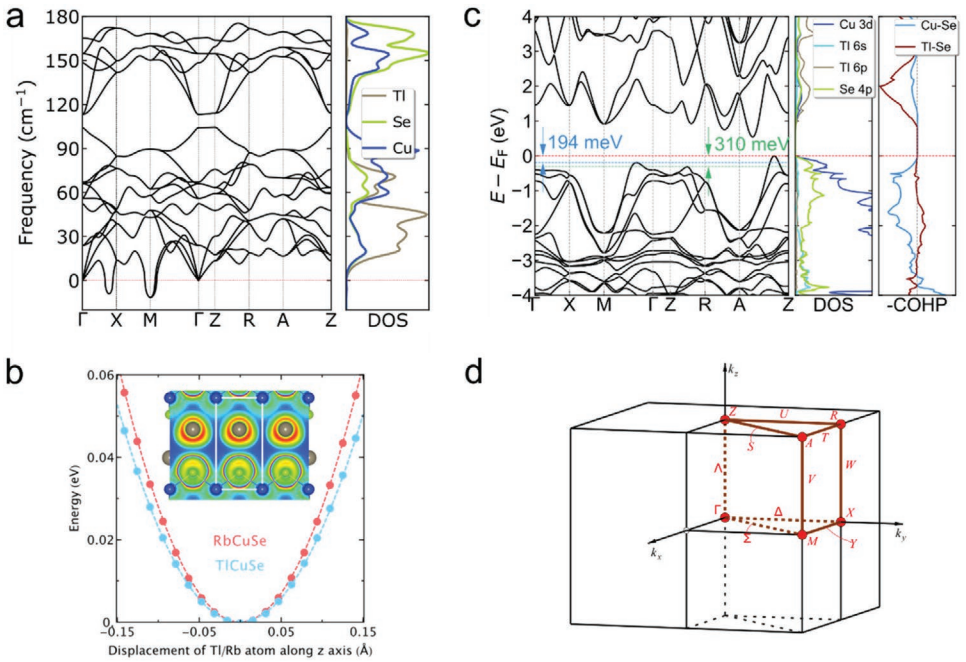

Figure 5. TlCuSe: a) phonon band structures along with phonon density of states at 0 K. b) Energy change (ΔE) of displacing Tl and Rb along *c*-axis with respect to the equilibrium position of TlCuSe and RbCuSe. The inset shows the electron localization function of TlCuSe. c) Electronic band structure, projected density of states, and the atom projected crystal orbital Hamilton population (COHP) of TlCuSe calculated with HSE06. Spin-orbit coupling is included in the band structure and DOS calculations but not in COHP. d) The first Brillouin zone of the *P*4/*nmm* space group.

(σ anti-bonding between s-orbitals).[24] Similarly, the hybridization between the 6p-orbitals of Tl^+ and the 4p-orbitals of Se shifts the CBM from the Γ to the S line. The strong p-d coupling between Cu 3d and Se 4p states can be clearly seen in the DOS and COHP of Figure 5c, which leads to filled anti-bonding levels below the Fermi level and weakened Cu−Se bonding, as noted above.[37a]

2.5. Thermoelectric Performance

Figure 6a shows the temperature dependent charge transport properties of TlCuSe measured along two different pressing directions. The electrical conductivity increases with rising temperature while the Seebeck coefficient decreases, which is typical for semiconductors. Since there is a preferential orientation of the layers perpendicular to the SPS pressing direction measurements were made both parallel and perpendicular to the pressing directions. For example, at 643 K, the electrical conductivity of the sample measured perpendicular (139 S cm^{-1}) to the pressing direction is more than twice higher than that measured parallel (47 S cm^{-1}) to it, consistent with the TlCuSe layers providing the primary carrier transport path.

The Seebeck coefficients are positive in the whole measured temperature range, indicating holes are the dominant charge carriers (Figure 6b). The Seebeck coefficient has a relatively large difference in the parallel and perpendicular directions, especially at high temperature. Such large Seebeck anisotropy is rare, so theoretical calculations were carried out to offer an insight into the origin of this anisotropy. The calculated Seebeck (S) coefficient as a function of the hole concentration is shown in Figure S6, Supporting Information. The calculated S at 300 K agrees with the experiment very well but is underestimated at the higher temperature, probably due to the uncertainty of the band gap and hole concentration at high temperature.

The Hall coefficient decreases rapidly as the carrier concentration N is thermally activated with increasing temperature, Figure 6c. The TlCuSe sample exhibits a self-doped p-type carrier concentration of $N = 5.9 \times 10^{18}$ cm^{-3} at room temperature, probably originating from Cu vacancies, and the carrier concentration sharply increases by two orders of magnitude with rising temperature (2.2×10^{20} cm^{-3} at 623 K) attributed to the onset of intrinsic carrier excitations. This is consistent with the positive Seebeck coefficient whose magnitude decreases with rising temperature. According to the Arrhenius-type equation, $N \propto e^{-E_g/2k_BT}$, in the intrinsic regime, we can extract a band gap energy E_g for TlCuSe of around 0.56 ± 0.03 eV (the inset in Figure 6d). The charge carrier mobility displayed in Figure 6f demonstrates that the scattering exponent ν in the mobility power law, $\mu \propto T^{\nu}$, begins around −3/2 near room temperature then drops ($\nu \leq -5/2$) at higher temperatures. Charge carrier scattering by acoustic phonons is therefore the dominant mechanism, with increased charge carrier effective mass playing a role at elevated temperatures.

Note that the measured hole concentration is based on the assumption of a single parabolic band, which is not the case in this compound. From our calculations, the observed anisotropy of S at high temperature is consistent with the experiment. At low temperature (300 K) and for low carrier concentrations (≈10^{19} cm^{-3}), the out-of-plane Seebeck coefficient ($S_{\parallel}$) is nearly the same as the in-plane one ($S_{\perp}$), and the system shows an

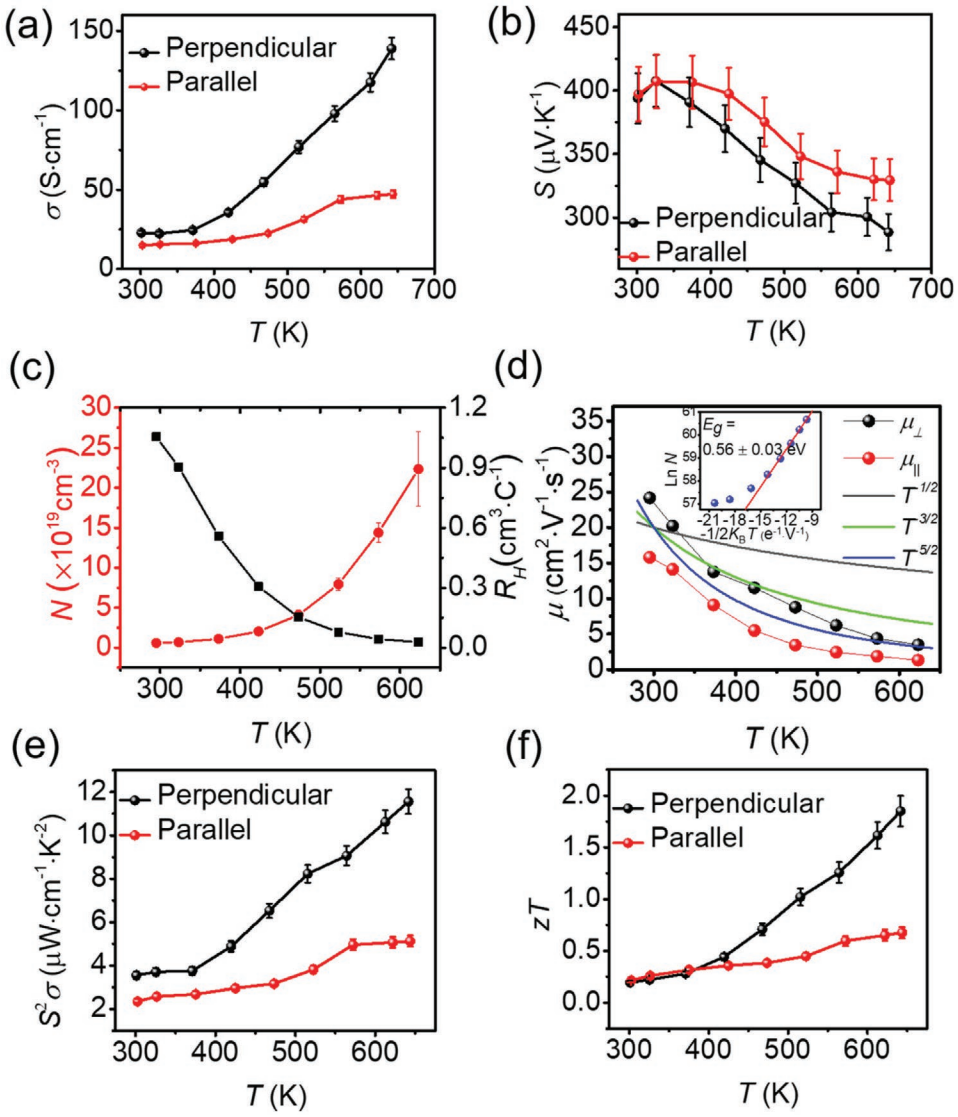

Figure 6. Temperature dependence of a) electrical conductivity, b) Seebeck coefficient, c) power factor, and d) the dimensionless *ZT* for TlCuSe measured parallel and perpendicular to the pressing directions. e) Temperature dependence of the carrier concentration and the Hall coefficient for TlCuSe. f) Temperature dependence of the charge carrier mobility. The inset is the fitting of activation energy based on the Arrhenius equation.

isotropic *S*. At higher temperature, for example, 600 K, and high hole concentration (due to thermal excitation), $S_{\perp}$ is obviously larger than $S_{\parallel}$ by the contribution from the top of the valence band (the peak along *A*-*Z* direction), see the inset of Figure S6b, Supporting Information. Within the rigid band approximation, Seebeck coefficient and electrical conductivity are given in Mott formula[40]

$$S = \frac{\pi^2}{3}\frac{k_B^2}{e}T\left[\frac{\mathrm{d}\ln\sigma(E)}{\mathrm{d}E}\right]_{E=E_F} \approx \frac{\pi^2}{3}\frac{k_B^2}{e}T\left[\frac{\mathrm{d}\ln N}{\mathrm{d}E}\right]_{E=E_F} \quad (2)$$

$$\sigma(E) = \frac{e^2}{3}\tau(E)v^2(E)N(E) \quad (3)$$

where k_B, $\tau(E)$, $v(E)$, $N(E)$ are the Boltzmann constant, energy-dependent relaxation time, carrier velocity, and density of states, respectively. Therefore, a large derivative of $N(E)$ with respect to E at the Fermi level leads to a large *S*. With the temperature and hole concentration increasing in TlCuSe, the Fermi level approaches the dispersive band along *A*-*Z* direction (see Figure S6, Supporting Information) and the change of the $N(E)$ with respect to E within the plane perpendicular to the layer direction decreases. However, the flat band along *Γ*-*Z* direction keeps a relatively large $\mathrm{d}(\ln N)/\mathrm{d}E$ and therefore a large *S* along the layer direction.

Because of the higher electrical conductivity perpendicular to the pressing direction, the power factor in this direction is much larger than that along the pressing direction, as shown in Figure 6e. The highest power factor of 11.6 W cm^{-1} K^{-2} was observed at 643 K which coupled with the ultralow thermal conductivity result in a very high *ZT* of 1.9 at 643 K (Figure 6f) perpendicular to the SPS pressing direction. It should be noted

that the TlCuSe materials in this study are not heavily doped nor optimized for best performance, and therefore further modulation of TlCuSe is warranted to achieve even higher *ZT*. Comparing with the best Cu-based thermoelectric materials such as Cu_2Se, TlCuSe does not seem to have a Cu migration issue, similar to the layered BiCuSeO. TlCuSe has a lower melting point than PbTe, which reaches the highest *ZT* at ≈1000 K, however, it has a lower intrinsic κ_L than both PbTe and Cu_2Se and therefore could achieve much higher *ZT* if could be further doped.

3. Conclusions

TlCuSe exhibits an ultralow lattice thermal conductivity (0.25 W $m^{-1}K^{-1}$) and a high power factor (11.6 μW cm^{-1} K^{-2}) at 643 K in the intrinsic semiconducting samples, which result in a high figure of merit *ZT* (1.9). DFT calculations uncover the complex mechanism underlying the low thermal conductivity of this compound: The weak chemical bonds between the constituent atoms, high average atomic mass, and strong anharmonicity from the lone-pair electrons of Tl^+ give rise to ultralow sound velocity and short phonon relaxation times. The lone-pair electrons Tl-$6s^2$ also modify the orbital character of the valence bands and push the valence band maximum away from the *Γ*-point, increasing the band degeneracy and therefore the power factor. The unique microscopic mechanisms uncovered in this compound could also inspire thermoelectric materials studies in the future.

4. Experimental Section

Electron Microscopy: Scanning/transmissionelectron microscopy (SEM/TEM) studies were carried out with a JEOL ARM300F GrandARM TEM operated at 300 kV and a JEOL 2100F TEM operated at 200 kV. TEM specimens were prepared using a FIB lift-out technique with a FEI Helios Nanolab SEM/FIB. Prior to FIB ion milling, a layer of amorphous carbon was deposited on the region of interest to protect its surface integrity. Bulk FIB milling techniques with Ga ion beam at 30 kV were used to reduce the specimen thickness to about 1μm. The specimens were then transferred with an Omniprobe to a molybdenum Lift-Out TEM Grid and further thinned with low energy Ga ions to achieve electron transparency with minimal ion-induced damage. To minimize damages by electron beam and any heat generated, the specimen was characterized at a cryogenic temperature (<123 K) using a Gatan Cryo-Transfer Holder. The specimen preparation and handling were performed in an Ar-filled glove box. A Wiener filter was applied to one of the high resolution TEM images using a HRTEM Filter Digital Micrograph script (http://www.dmscripting.com/hrtem_filter.html).

Electrical Properties: The SPS-processed pellets (dimension: 3 × 3 × 10 mm^3) of TlCuSe were cut into bars both perpendicular and parallel to the sintering pressure directions for electrical property measurement. The samples were spray-coated with boron nitride film to minimize outgassing while heating, except places needed for electrical contact with the thermocouples, heater, and voltage probes. The Seebeck coefficients and electrical conductivities were measured simultaneously with an Ulvac Riko ZEM-3 instrument under a low-pressure helium atmosphere and a temperature ranging from room temperature to 633 K. The uncertainty of the measured Seebeck coefficient and electrical conductivity is about 5%.[41]

Thermal Conductivity: The thermal diffusivity coefficient (*D*) measurements were conducted with the samples with a dimension of 6.00 × 6.00 × 1.00 mm^3, as shown in Figure S7, Supporting Information. The thermal diffusivities on samples cut both perpendicular and parallel to the sintering pressure directions were measured by using Netzsch LFA457 instrument. The samples were coated with graphite for a uniform heat emissivity over the whole sample area. A Cowan model with pulse correction was used for the thermal diffusivity analysis. The total thermal conductivity was calculated by the equation $\kappa_{tot} = DC_p d$, where *d* is the density calculated by using the mass and the volume of the sample. The specific heat (C_p) was calculated by the Dulong–Petit law $C_p = 3R/\overline{M}$, where *R* is the gas constant 8.314 J mol^{-1} K^{-1} and $\overline{M}$ is the average molar mass of TlCuSe. The uncertainty of the thermal conductivity was estimated to be within 8% and the uncertainty in calculation of *ZT* was 15%.[41] Thermal conductivity (κ_{tot}) is composed of two contributions, electrical thermal conductivity (κ_{ele}) and lattice thermal conductivity (κ_{lat}). The lattice thermal conductivity can be obtained by subtracting κ_{ele} from κ_{total}.

$$\kappa_{lat} = \kappa_{tot} - \kappa_{ele} = \kappa_{tot} - L\sigma T \tag{4}$$

Here, κ_{ele} is estimated by the Wiedemann–Franz relation: $\kappa_{ele} = L\sigma T$, where σ is the electrical conductivity and *L* is the Lorenz number. Assuming a single parabolic band model, the Lorenz number *L* is calculated as[42]

$$L = \left(\frac{k_B}{e}\right)^2 \left[\frac{(r+7/2)F_{r+5/2}(\eta)}{(r+3/2)F_{r+1/2}(\eta)} - \left[\frac{(r+5/2)F_{r+3/2}(\eta)}{(r+3/2)F_{r+1/2}(\eta)}\right]^2\right] \tag{5}$$

Here, the reduced Fermi energy η can be obtained from the Seebeck coefficient as

$$\alpha = \pm\frac{k_B}{e}\left[\frac{(r+5/2)F_{r+3/2}(\eta)}{(r+3/2)F_{r+1/2}(\eta)} - \eta\right] \tag{6}$$

$$F_n(\eta) = \int_\infty^0 \frac{\chi^n}{1+e^{\chi-\eta}} d\chi \tag{7}$$

where k_B is the Boltzmann constant, *e* is the electron charge, α is the Seebeck coefficient, and *r* is the scattering factor; here, $r = -1/2$ for charge carrier scattering by acoustic phonons.

Hall Measurements: The Hall coefficient measurement was performed by a homebuilt system using an AC 4-probe method with excitation magnetic fields of +0.5 and −0.5 T. The system used an air-bore, helium-cooled superconducting magnet to generate the field within a high temperature oven that surrounds the Ar gas-filled sample probe. The carrier density was calculated from the Hall coefficient assuming a single carrier, that is, $n = 1/R_H$, where R_H is the Hall coefficient. The estimated error of the measurement was around 3% at the 10^{19} cm^{-3} level of carrier density but becomes larger at the 10^{20} cm^{-3} level based on the standard deviation of several data points at a single temperature. The charge carrier mobility was calculated as $\mu = \sigma R_H$.

Temperature-Dependent Heat Capacity Measurements: Heat capacity was measured using a Dynacool Physical Property Measurement System (PPMS, Quantum Design) between 1.8 and 300 K. Apiezon N grease was used to fix polycrystalline samples prepared by SPS to the sample stage.

Computational Methods: All DFT calculations were performed using the Vienna ab initio Simulation Package (VASP),[43] with a plane wave basis set and projector-augmented wave (PAW) pseudo potentials.[44,45] The PBEsol functional was used for crystal structure relaxation and phonon related properties calculations,[46] which yielded lattice constants of $a = b = 4.00$ Å and $c = 8.21$ Å. The screened hybrid functional HSE06 was adopted for electronic structure calculations.[47,48] SOC was included. The second force constants were computed by using the Phonopy,[49] with 4 × 4 × 2 supercells (192 atoms). The phonon spectra at room-temperature was computed with the self-consistent phonon approximation, which comprised the first-order correction from quartic anharmonicity.[50] The third and fourth-order force constants were calculated by using the compressive sensing lattice dynamics.[51] The lattice thermal conductivity was calculated by solving the linearized

Boltzmann transport equation using ShengBTE.[52] The average speed of sound (v_a) was calculated from bulk (B) and shear (G) moduli as[53]

$$v_a = \left[\frac{1}{3}\left(\frac{1}{v_L^3} + \frac{2}{v_T^3}\right)\right]^{-1/3} \tag{8}$$

$$v_T = \sqrt{\frac{G}{\rho}} \tag{9}$$

$$v_L = \sqrt{\frac{B + \frac{4}{3}G}{\rho}} \tag{10}$$

where v_L and v_T are longitudinal and transversal sound velocities, respectively. ρ is the mass density. B and G are calculated from elastic constants.

Supporting Information

Supporting Information is available from the Wiley Online Library or from the author.

Acknowledgements

This work was supported in part by a grant from the U.S. Department of Energy, Office of Science, and Office of Basic Energy Sciences under Award Number DE-SC0014520 (synthesis and characterization of thermoelectric materials). The authors acknowledge the computing resources provided by the National Energy Research Scientific Computing Center (NERSC), a U.S. Department of Energy Office of Science User Facility operated under Contract No. DE-AC02-05CH11231 (heat capacity measurements).

Conflict of Interest

The authors declare no conflict of interest.

Data Availability Statement

The data that supports the findings of this study are available in the supplementary material of this article.

Keywords

chalcogenides, narrow-gap semiconductors, thermal conductivity, thermoelectric materials

Received: June 26, 2021
Revised: August 2, 2021
Published online: September 14, 2021

[1] Y. B. Luo, Y. Zheng, Z. Z. Luo, S. Q. Hao, C. F. Du, Q. H. Liang, Z. Li, K. A. Khor, K. Hippalgaonkar, J. W. Xu, Q. Y. Yan, C. Wolverton, M. G. Kanatzidis, *Adv. Energy Mater.* **2018**, *8*, 1702167.

[2] a) G. Tan, L.-D. Zhao, M. G. Kanatzidis, *Chem. Rev.* **2016**, *116*, 12123; b) T. M. Tritt, M. Subramanian, *MRS Bull.* **2006**, *31*, 188; c) G. Chen, M. Dresselhaus, G. Dresselhaus, J.-P. Fleurial, T. Caillat, *Int. Mater. Rev.* **2003**, *48*, 45; d) J. He, T. M. Tritt, *Science* **2017**, *357*, 1369.

[3] a) Y. Pei, X. Shi, A. LaLonde, H. Wang, L. Chen, G. J. Snyder, *Nature* **2011**, *473*, 66; b) Y. Pei, H. Wang, G. J. Snyder, *Adv. Mater.* **2012**, *24*, 6125.

[4] a) J. P. Heremans, B. Wiendlocha, A. M. Chamoire, *Energy Environ. Sci.* **2012**, *5*, 5510; b) G. Mahan, J. Sofo, *Proc. Natl. Acad. Sci. U. S. A.* **1996**, *93*, 7436.

[5] a) M. Dresselhaus, G. Dresselhaus, X. Sun, Z. Zhang, S. Cronin, T. Koga, *Phys. Solid State* **1999**, *41*, 679; b) T. Harman, P. Taylor, M. Walsh, B. LaForge, *Science* **2002**, *297*, 2229.

[6] Z. Liu, J. Mao, T.-H. Liu, G. Chen, Z. Ren, *MRS Bull.* **2018**, *43*, 181.

[7] E. Quarez, K.-F. Hsu, R. Pcionek, N. Frangis, E. Polychroniadis, M. G. Kanatzidis, *J. Am. Chem. Soc.* **2005**, *127*, 9177.

[8] A. Minnich, M. S. Dresselhaus, Z. Ren, G. Chen, *Energy Environ. Sci.* **2009**, *2*, 466.

[9] K. Biswas, J. Q. He, I. D. Blum, C. I. Wu, T. P. Hogan, D. N. Seidman, V. P. Dravid, M. G. Kanatzidis, *Nature* **2012**, *489*, 414.

[10] D. Bilc, S. D. Mahanti, E. Quarez, K. F. Hsu, R. Pcionek, M. G. Kanatzidis, *Phys. Rev. Lett.* **2004**, *93*, 146403.

[11] a) L. D. Zhao, S. H. Lo, Y. S. Zhang, H. Sun, G. J. Tan, C. Uher, C. Wolverton, V. P. Dravid, M. G. Kanatzidis, *Nature* **2014**, *508*, 373; b) C. Zhou, Y. K. Lee, Y. Yu, S. Byun, Z.-Z. Luo, H. Lee, B. Ge, Y.-L. Lee, X. Chen, J. Y. Lee, O. Cojocaru-Miređin, H. Chang, J. Im, S.-P. Cho, M. Wuttig, V. P. Dravid, M. G. Kanatzidis, *Nat. Mater.* **2021**, https://doi.org/10.1038/s41563-021-01064-6.

[12] C. G. Fu, S. Q. Bai, Y. T. Liu, Y. S. Tang, L. D. Chen, X. B. Zhao, T. J. Zhu, *Nat. Commun.* **2015**, *6*, 8144.

[13] A. A. Olvera, N. A. Moroz, P. Sahoo, P. Ren, T. P. Bailey, A. A. Page, C. Uher, P. F. P. Poudeu, *Energy Environ. Sci.* **2017**, *10*, 1668.

[14] X. Shi, J. Yang, J. R. Salvador, M. F. Chi, J. Y. Cho, H. Wang, S. Q. Bai, J. H. Yang, W. Q. Zhang, L. D. Chen, *J. Am. Chem. Soc.* **2011**, *133*, 7837.

[15] a) K. F. Hsu, D. Y. Chung, S. Lai, A. Mrotzek, T. Kyratsi, T. Hogan, M. G. Kanatzidis, *J. Am. Chem. Soc.* **2002**, *124*, 2410; b) K. Kovnir, E. S. Toberer, *Chem. Mater.* **2016**, *28*, 2463.

[16] T. M. Tritt, *Thermal Conductivity: Theory, Properties, and Applications*, Springer Science & Business Media, Berlin, Germany **2005**.

[17] D. T. Morelli, V. Jovovic, J. P. Heremans, *Phys. Rev. Lett.* **2008**, *101*, 035901.

[18] M. Christensen, A. B. Abrahamsen, N. B. Christensen, F. Juranyi, N. H. Andersen, K. Lefmann, J. Andreasson, C. R. Bahl, B. B. Iversen, *Nat. Mater.* **2008**, *7*, 811.

[19] H. L. Liu, X. Shi, F. F. Xu, L. L. Zhang, W. Q. Zhang, L. D. Chen, Q. Li, C. Uher, T. Day, G. J. Snyder, *Nat. Mater.* **2012**, *11*, 422.

[20] a) R. Hanus, M. T. Agne, A. J. Rettie, Z. Chen, G. Tan, D. Y. Chung, M. G. Kanatzidis, Y. Pei, P. W. Voorhees, G. J. Snyder, *Adv. Mater.* **2019**, *31*, 1900108; b) W. Li, S. Lin, B. Ge, J. Yang, W. Zhang, Y. Pei, *Adv. Sci.* **2016**, *3*, 1600196; c) W. G. Zeier, A. Zevalkink, Z. M. Gibbs, G. Hautier, M. G. Kanatzidis, G. J. Snyder, *Angew. Chem., Int. Ed.* **2016**, *55*, 6826.

[21] M. K. Jana, K. Pal, A. Warankar, P. Mandal, U. V. Waghmare, K. Biswas, *J. Am. Chem. Soc.* **2017**, *139*, 4350.

[22] M. K. Jana, K. Pal, U. V. Waghmare, K. Biswas, *Angew. Chem.* **2016**, *128*, 7923.

[23] H. Xie, S. Hao, J. Bao, T. J. Slade, G. J. Snyder, C. Wolverton, M. G. Kanatzidis, *J. Am. Chem. Soc.* **2020**, *142*, 9553.

[24] R. Hoffmann, *Angew. Chem.* **1987**, *99*, 871.

[25] S.-H. Wei, A. Zunger, *Phys. Rev. B* **1997**, *55*, 13605.

[26] L.-D. Zhao, J. He, D. Berardan, Y. Lin, J.-F. Li, C.-W. Nan, N. Dragoe, *Energy Environ. Sci.* **2014**, *7*, 2900.

[27] J. G. He, Y. Xia, S. S. Naghavi, V. Ozolins, C. Wolverton, *Nat. Commun.* **2019**, *10*, 719.

[28] R. Berger, *J. Solid State Chem.* **1987**, *70*, 65.

[29] T. Takabatake, K. Suekuni, T. Nakayama, *Rev. Mod. Phys.* **2014**, *86*, 669.

[30] a) S. Pailhès, H. Euchner, V. M. Giordano, R. Debord, A. Assy, S. Gomès, A. Bosak, D. Machon, S. Paschen, M. De Boissieu, *Phys.*

Rev. Lett. **2014**, *113*, 025506; b) T. Tadano, Y. Gohda, S. Tsuneyuki, *Phys. Rev. Lett.* **2015**, *114*, 095501; c) C. Chang, A. Fennimore, A. Afanasiev, D. Okawa, T. Ikuno, H. Garcia, D. Li, A. Majumdar, A. Zettl, *Phys. Rev. Lett.* **2006**, *97*, 085901.

[31] a) P. J. Ying, X. Li, Y. C. Wang, J. Yang, C. G. Fu, W. Q. Zhang, X. B. Zhao, T. J. Zhu, *Adv. Funct. Mater.* **2017**, *27*, 1604145; b) E. J. Skoug, D. T. Morelli, *Phys. Rev. Lett.* **2011**, *107*, 235901; c) G. Zheng, X. L. Su, H. Y. Xie, Y. J. Shu, T. Liang, X. Y. She, W. Liu, Y. G. Yan, Q. J. Zhang, C. Uher, M. G. Kanatzidis, X. F. Tang, *Energy Environ. Sci.* **2017**, *10*, 2638.

[32] T. Zhu, S. Zhang, S. Yang, X. Zhao, *Phys. Status Solidi R* **2010**, *4*, 317.

[33] Y. Xia, V. I. Hegde, K. Pal, X. Hua, D. Gaines, S. Patel, J. He, M. Aykol, C. Wolverton, *Phys. Rev. X* **2020**, *10*, 041029.

[34] D. Spitzer, *J. Phys. Chem. Solids* **1970**, *31*, 19.

[35] E. S. Toberer, A. Zevalkink, G. J. Snyder, *J. Mater. Chem.* **2011**, *21*, 15843.

[36] L. Pauling, *J. Am. Chem. Soc.* **1929**, *51*, 1010.

[37] a) S.-H. Wei, A. Zunger, *Phys. Rev. B* **1988**, *37*, 8958; b) Y. Zhang, L. Xi, Y. Wang, J. Zhang, P. Zhang, W. Zhang, *Comput. Mater. Sci.* **2015**, *108*, 239.

[38] P. Qiu, X. Shi, L. Chen, *Energy Storage Mater.* **2016**, *3*, 85.

[39] a) Y. Z. Pei, X. Y. Shi, A. LaLonde, H. Wang, L. D. Chen, G. J. Snyder, *Nature* **2011**, *473*, 66; b) M. Aykol, S. Kim, V. I. Hegde, S. Kirklin, C. Wolverton, *Phys. Rev. Mater.* **2019**, *3*, 025402.

[40] a) N. F. Mott, E. A. Davis, *Electronic Processes in Non-crystalline Materials*, Oxford University Press, Oxford **2012** b) M. Cutler, N. F. Mott, *Phys. Rev.* **1969**, *181*, 1336.

[41] J. de Boor, S. Gupta, H. Kolb, T. Dasgupta, E. Muller, *J. Mater. Chem. C* **2015**, *3*, 10467.

[42] a) L. D. Zhao, S. H. Lo, J. Q. He, H. Li, K. Biswas, J. Androulakis, C. I. Wu, T. P. Hogan, D. Y. Chung, V. P. Dravid, M. G. Kanatzidis, *J. Am. Chem. Soc.* **2011**, *133*, 20476; b) J. Androulakis, S. C. Peter, H. Li, C. D. Malliakas, J. A. Peters, Z. F. Liu, B. W. Wessels, J. H. Song, H. Jin, A. J. Freeman, M. G. Kanatzidis, *Adv. Mater.* **2011**, *23*, 4163.

[43] a) G. Kresse, J. Hafner, *Phys. Rev. B* **1993**, *48*, 13115; b) G. Kresse, J. Furthmuller, *Comput. Mater. Sci* **1996**, *6*, 15.

[44] P. E. Blöchl, *Phys. Rev. B* **1994**, *50*, 17953.

[45] G. Kresse, D. Joubert, *Phys. Rev. B* **1999**, *59*, 1758.

[46] J. P. Perdew, A. Ruzsinszky, G. I. Csonka, O. A. Vydrov, G. E. Scuseria, L. A. Constantin, X. Zhou, K. Burke, *Phys. Rev. Lett.* **2008**, *100*, 136406.

[47] J. Heyd, G. E. Scuseria, M. Ernzerhof, *J. Chem. Phys.* **2003**, *118*, 8207.

[48] J. Heyd, G. E. Scuseria, M. Ernzerhof, *J. Chem. Phys.* **2006**, *124*, 219906.

[49] A. Togo, I. Tanaka, *Scr. Mater.* **2015**, *108*, 1.

[50] a) D. Hooton, *London, Edinburgh Dublin Philos. Mag. J. Sci.* **1955**, *46*, 422; b) T. R. Koehler, *Phys. Rev. Lett.* **1966**, *17*, 89; c) N. Werthamer, *Phys. Rev. B* **1970**, *1*, 572; d) M. Klein, G. Horton, *J. Low Temp. Phys.* **1972**, *9*, 151.

[51] F. Zhou, W. Nielson, Y. Xia, V. Ozoliņš, *Phys. Rev. Lett.* **2014**, *113*, 185501.

[52] W. Li, J. Carrete, N. A. Katcho, N. Mingo, *Comput. Phys. Commun.* **2014**, *185*, 1747.

[53] R. Hill, *Proc. Phys. Soc., London, Sect. A* **1952**, *65*, 349.